Cryostat exit detectors for $\mathbf{G}^0$

A thesis submitted in partial fulfillment of the requirement
for the degree of Bachelor of Science in
Physics from the College of William and Mary in Virginia,

by

Anela O. Rayfield

Advisor: Prof. David S. Armstrong

Williamsburg, Virginia
May 2004

Contents

Acknowledgments

I would like to thank The Department of Physics at The College of William and Mary, my fellow W&M graduate students and dear friends Stephanie-Louise Bailey and Sabine Fuchs, undergraduate student from University Of British Columbia Michael Choi, Post-docs Gary Rutledge, Fatha Benmokhtar, and Michael Gericke, and most importantly Dr. David Armstrong. All have showed me what hard work and research can achieve. I have gained important traits from those whom I have been privileged to work with. These traits will benefit me through my journey of life, both professionally and personally. Last, but not the least, I would like to thank my husband Richard Rayfield for always being there for me. I could not have made this far without him.

List of Figures

List of Tables

Abstract

The G^0 collaboration at Jefferson Laboratory will examine the contributions of the strange and anti-strange quarks to the fundamental properties of the proton by measuring parity-violating electron scattering at backward angles. The results acquired from the G^0 backward angle experiment and the previously done forward angle electron scattering measurements will allow us to determine how $s\bar{s}$ pairs affect the distribution of electric charge and magnetization of the proton. The main goal of this thesis is to assemble the cryostat exit detectors (CED) needed for this experiment and test their performance for the parity-violating electron scattering experiment. We used radiation sources (Na-22) and cosmic rays to test these detectors.

Chapter 1

Physics of the G^0 Experiment

1.1 Elementary particles

Present evidence indicates that matter is built from two types of fundamental fermions, called quarks and leptons, which are structureless and point-like on a scale of 10^{-17}m [1]. Quarks can have electric charge $+\frac{2}{3}e$ and $-\frac{1}{3}e$. They occur in several different 'flavors' which are labeled as u(up),d(down),s(strange),c(charm),b(bottom), and t(top). For each quark there is the anti-quark with the opposite sign of electric charge and strangeness.

Particles built from two types of quark combination, such as

Baryon=qqq (three quarks) and Meson=$q\bar{q}$ (quark-anti-quark pair),

are called hadrons. For example, the proton and neutron are baryons with the basic quark distribution

p(proton)=uud and n(neutron)=udd

valence quarks. In addition to the 3 valence quarks in a baryon there is a "sea" of $q\bar{q}$ pairs. The $q\bar{q}$ pairs have a short time life and they are formed only when the conservation of energy is temporarily violated, as allowed by the Heisenberg uncertainty principle.

1

1.2 Quantum Chromodynamics

Quantum chromodynamics (QCD) is the formal gauge theory of the strong color interactions between quarks [1]. Red, blue, or green are the three possible values of the color charge of a quark. In contrast, anti-quarks carry anti-color. The color charge of the strong quark interaction is analogous to the electric charge in the electromagnetic interaction. QCD involves the force between colored quarks due to the exchange of gluons, in analogy with quantum electrodynamics in which charged objects interact due to the exchange of photons.
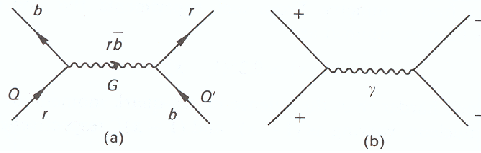
Figure 1.1: Feynman Diagrams: a) gluon exchange-quantum chromodynamics; b) photon exchange-quantum electrodynamics).

1.3 Form Factors

Since QCD is charge independent and helicity (the spin projection on the direction of the momentum) dependent, we will be able to extract the form factors G_E^S and G_M^S. The G^0 form factor appears only through weak interaction (Z^0) with proton. The cross-section for scattering by an extended target can be written in terms of that for a point target by the inclusion of a "form factor" $F(q)$ [2]. The G_E and G_M are form factors related to the charge and magnetic moment distributions in the proton. The strange quark effects on the electromagnetic structure of the nucleon are measured by the form factors G_E^S and G_M^S. Hence, the question is: do $s\bar{s}$ quarks contribute to the proton's structure and how significant is their contribution to the

electric and magnetic properties of the proton?

1.4 Parity-Violating electron scattering

If the electron − proton elastic scattering is done using polarized electrons and if only one virtual photon exchange is involved, the cross section σ would not depend on the helicity of the electron (the spin projection on the direction of the momentum) [3]. The electromagnetic interaction is thus parity conserving. However, since both the electromagnetic (photon exchange) and the weak (Z exchange) forces contribute to electron scattering, the counting rate is proportional to the sum of the 2 amplitudes squared $|M_Z + M_\gamma|^2$, where M_γ is the electromagnetic interaction amplitude and M_Z is the weak interaction amplitude. Because the parity-violating terms in the cross sections are proportional to the electron helicity, the terms M_γ^2 and M_Z^2 cancel in the difference between the counting rates measured for positive and negative helicity states (only the cross term $M_\gamma M_Z$ remains) whereas they remain in the sum of these rates. We then can calculate and measure the asymmetry, even if it is small, which is given by (neglecting the M_Z^2 term in the denominator):

$$A = \frac{N_+ - N_-}{N_+ + N_-} \propto \frac{M_\gamma M_Z}{M_Z^2} \simeq 50 \times 10^{-6}$$

where N_+ is the number of scattered particles for the positive helicity configuration and N_- is the number of scattered particles for the negative helicity configuration. From the measured asymmetry we will be able to determine electric and magnetic form factors G_E and G_M.

Chapter 2

G^0 system description

2.1 G^0 detector

The G^0 detector will be composed of 8 octants. Each octant for the backward angle experiment will have Focal Plane detectors (FPD), Cryostat exit detectors (CED) and Cerenkov detectors.The octants will be mounted and symmetrically arranged around the electron beamline axis. Four of the octants will be assembled of parts from the North American collaboration and the other four from the French collaboration. Each octant contains 9 cryostat exit detectors, which are plastic scintillation detectors. Each scintillation detector has two acrylic lightguides at each end. The ends of the lightguides are connected to photomultiplier tubes. The scintillation light produced when a scattered electron strikes the CED is transported via the lightguides to the photomultiplier tubes where it is converted to an electrical signal. In this way, the number of electrons scattered into a particular CED can be measured. This thesis will mainly focus on the assembling and testing of the CED detectors.

2.2 Scintillation Detectors

The function of scintillators is to detect ionizing radiation. The ideal scintillator should convert linearly the kinetic energy of charged particles into detectable light
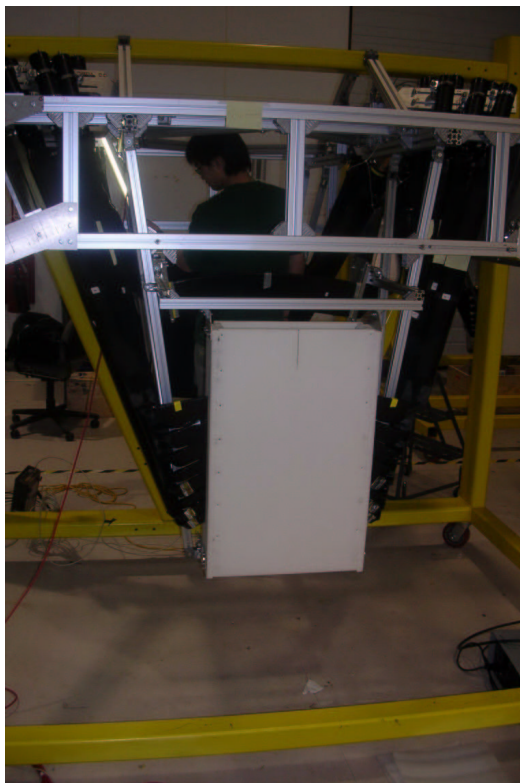
Figure 2.1: Octant 8 assembled.

with a high efficiency. The scintillation material should be transparent to the wavelength of its own emission for good light collection, permit a short decay time of the induced luminescence so that fast signal pulses can be generated, and have an index of refraction near that of glass (~ 1.5) to allow efficient coupling of the scintillation light to a photomultiplier tube [4]. Charged particles interact electromagnetically with electrons and they ionize atoms or molecules when passing through the scintillation material. The free electrons combine with the ions to form neutral pairs that are initially in an excited state. Hence, when these excited states decay, one or more near ultraviolet or visible photons are produced. In the G^0 experiment, the visible photons travel through the scintillators and lightguides. The photon's attenuation is small when it passes through this material. However, their number is not sufficient

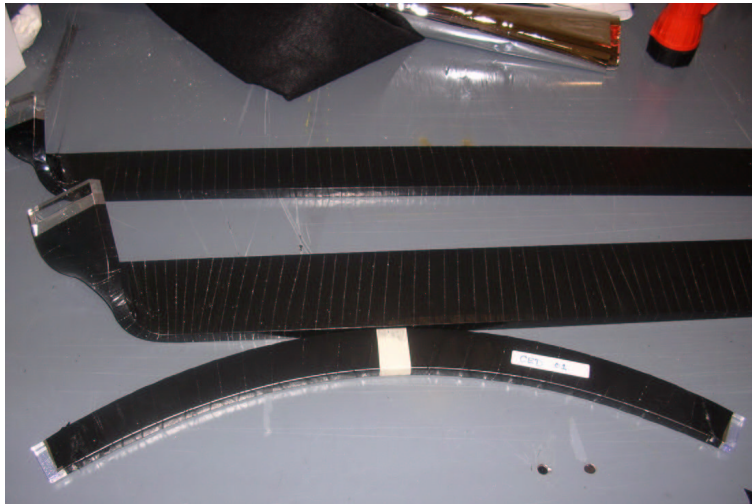on their own to be converted to a reasonable electrical signal.

Figure 2.2: Lightgudes and arc-shaped scintillator .

2.3   Photomultiplier tubes

A photomultiplier tube (PMT) converts the extremely weak light output of a scintillation pulse, no more than a few hundred photons, into a corresponding electrical signal. The two major elements of a PMT consist of a photosensitive layer, called a photocathode, coupled to an electron multiplier structure. The photocathode converts as many of the incident photons as possible into low-energy electrons by the photoelectric effect. These electrons are not of sufficient number or energy to be detected by standard electronics. The electron multiplier serves as an amplifier to increase their number. After amplification through the PMT, a scintillation pulse typically contains between 10^7 and 10^{10} electrons which is sufficient as the charge signal for the original scintillation event.

Chapter 3

CED construction

The backward-angle 2nd phase of the G^0 experiment requires major assembly and testing of different elements in the composition of the main detector. So far, we assembled completely eight octants of CED detectors that will be used in the G^0 experiment. Assembling and testing various elements of each octant requires precision and is time demanding. For example, we had to connect adapters to each lightguide and to wrap the lightguides with three or more layers of different tape in order to prevent any "light leak". In addition, we connected two PMT's to each lightguide. Before we connected the lightguides to each scintillator, we had to make Rohacell boxes to support eight of the nine scintillators (CEDs). ROHACELL is a polymethacrylimide- (PMI-) hard foam, that is used as a core material for sandwich constructions. It shows outstanding mechanical and thermal properties. In comparison to all other foams it offers the best ratio of weight and mechanical properties as well as highest heat resistance. The CED 9 is assembled outside of the box. Finally, the system comprised of lightguides, PMT's and the box with scintillators had to be mounted on metal brackets and aligned carefully before connecting the whole. While we are assembling the parts, we tested the completed octant and looked for further lightleaks in the system and checked the scintillators for their performing efficiency.

The "light leak" is unwanted light that would produce extra, spurious signals

which would distort the important data. We tested scintillators for light tightness by connecting the scintillator panel to an oscilloscope and a voltage source. With the scintillator covered with a piece of black fabric and exposed to a fluorescent flash light, we found the signal with the oscilloscope. If there was a light leak, the signal displayed on the oscilloscope would increase. The light leak area of the scintillator was identified and the scintillator was re-taped and re-checked again. If there was no signal increase, then the scintillator is light tight.

Beside the light tightness of the scintillators our main concern was the scintillating surface condition. A cracked surface or "crazing" would give us an unwanted reduction in the total internal reflection because the photons are mainly transported to the lightguide via total internal reflection. Our goals are to have the number of photoelectrons greater than the minimum required to record the event, to ensure that that the number of photoelectrons for electrons that strike any location in the scintillator is good over the entire detector, and that both the left and right PMT's coincidence ensures a true event. We have used cosmic rays for testing. Figure 3.1 shows a typical pulse-hight spectrum for cosmic rays as measured in one of the PMT's for one CED.
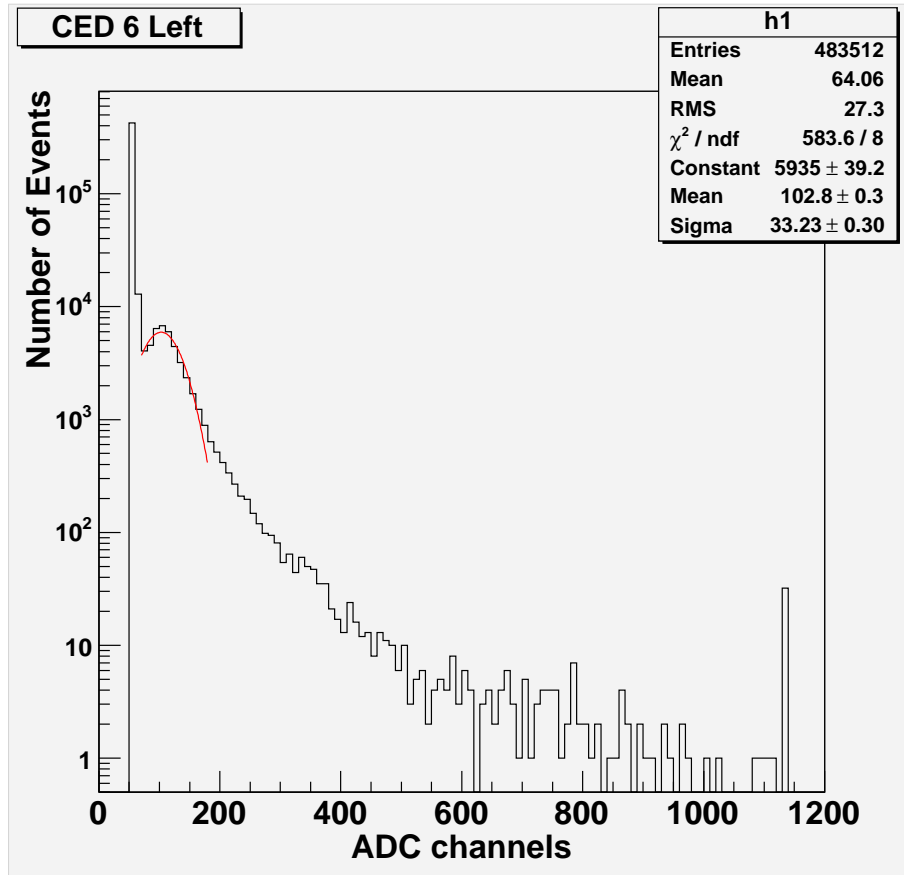
Figure 3.1: Pulse Height Spectrum for CED 6 Left for cosmic rays. A Gaussian fit to a limited range of the spectrum is superimposed representing, the minimum-ionizing peak. The ADC pedestal is at channel 60. The pedestal is due to background noise caused by electronics and the ADC module. The ADC stands for analog-to digital converter, which converts continuous signal (voltage) to digital number.

From Figs. 3.1, 3.2, 3.3 and 3.4 we notice that the minimum-ionizing cosmic ray peaks differ from one another. The reason for this variation is due to variations in the photocathode efficiency of each photomultiplier tube and multiplication of electrons inside of photomultiplier tube. The photocathode efficiency is determined by the ratio of the number of electrons and number of photons. Additionally, in the process of multiplication of electrons, when the accelerated electrons from the photocatode hit the surface of the dynode in the photomultiplier tube, the energy deposited by
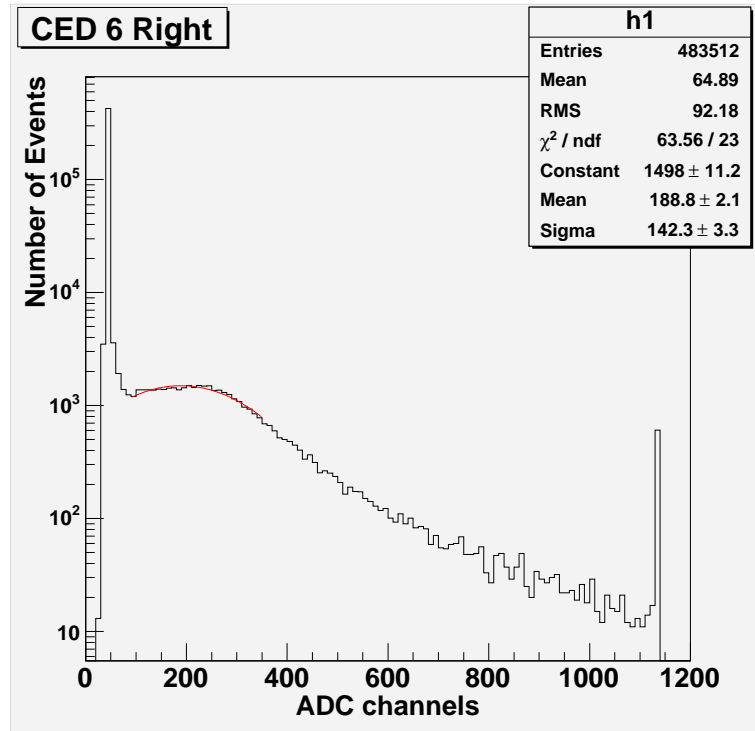
9

Figure 3.2: Pulse Height Spectrum (ADC) for CED 6 Right for cosmic rays.

the incident electron results in reemission of more than one electron from the same surface. For each photomultiplier tube the dynodes do not have the same ability to multiply and to accelerate the electrons, thus, the number of re-emitted electrons depends on the interdynode voltages. Each interdynode voltage depends on the high voltage provided by the power supply and the resistances in the resistor chain in the PMT. Since the overall gain of each PMT is different we will have to adjust the electronics.
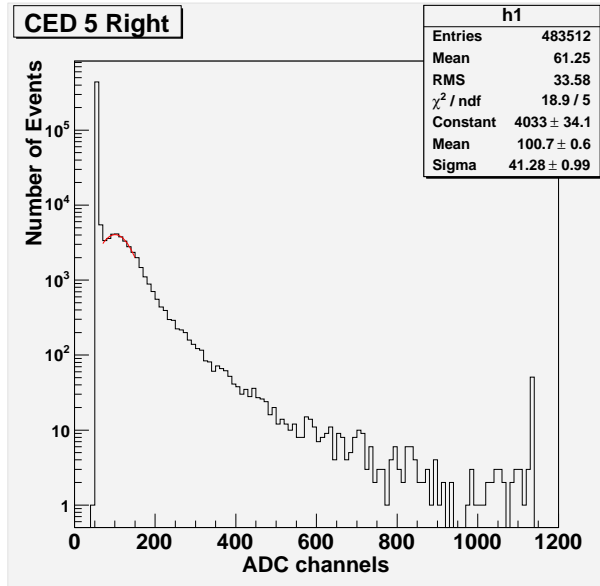
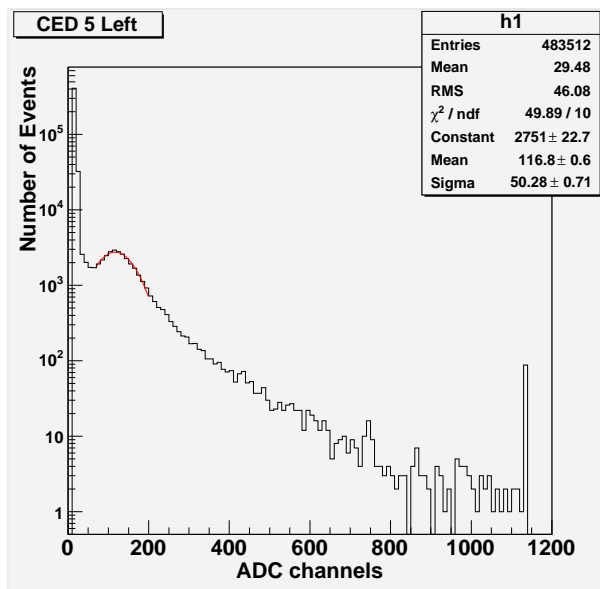Figure 3.3: Pulse Height Spectrum (ADC) for CED 5 Right for cosmic rays.

Figure 3.4: Pulse Height Spectrum (ADC) for CED 5 Left for cosmic rays.

Chapter 4

Electronics

For the CED testing setup, a valid event occurs when a cosmic ray traverses the four trigger counters with a pulse height over the value set by the discriminator threshold. In our test setup the trigger counters consisted of four large paddles made of scintillators, where two of them are aligned parallel to the floor and two are perpendicular to the floor. In Figs. 4.1 and 4.2 the discriminator will examine an electrical pulse and determine whether it is large enough to be considered as an actual signal or noise. If the signal is above the threshold, the discriminator sends an output logic signal to the coincidence unit (logical AND). If the coincidence unit receives the signal from both PMTs at the same time it will send a signal not only to the Time-to-digital converter (TDC), but also to the ADC. A TDC module records the time difference between start and stop pulses and tells us when the coincidence occurred. A start signal is defined by the coincidence unit. When the signal is sent to the ADC it tells the ADC gate to open and to start measuring the analog pulse from the PMT directly. The amount of charge collected while the ADC gate is open is integrated and recorded in the ADC histogram. We used the CAMAC system as the interface between our setup and a computer. We used the Computer Automated Measurement And Control, (CAMAC), as the interface between our setup and a computer. CAMAC is a modular data handling system used at almost every nuclear

physics research laboratory. CAMAC takes digital data from ADC and TDC and sends it to the computer. This is the electronics schematic for cosmic rays and the single photoelectron.

G0 CED Circuit Diagram
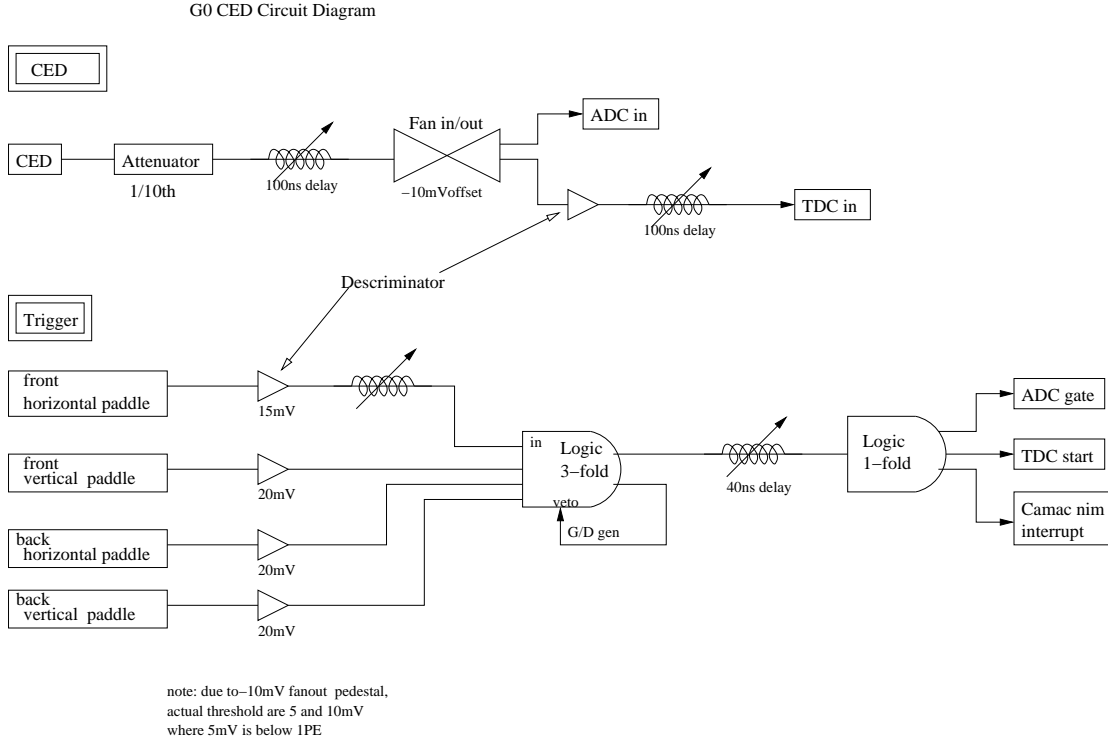
Figure 4.1: Electronic diagram for Cosmic Ray data-taking.

For the SPE setup, we could not use trigger counters to start TDC and gate ADC, because we are looking for events that are noise in the CED or PMT, so they would not be co-related with a signal in a trigger counter. Therefore, we need to use the PMT signal itself to generate the TDC start and ADC gate. The veto input to the
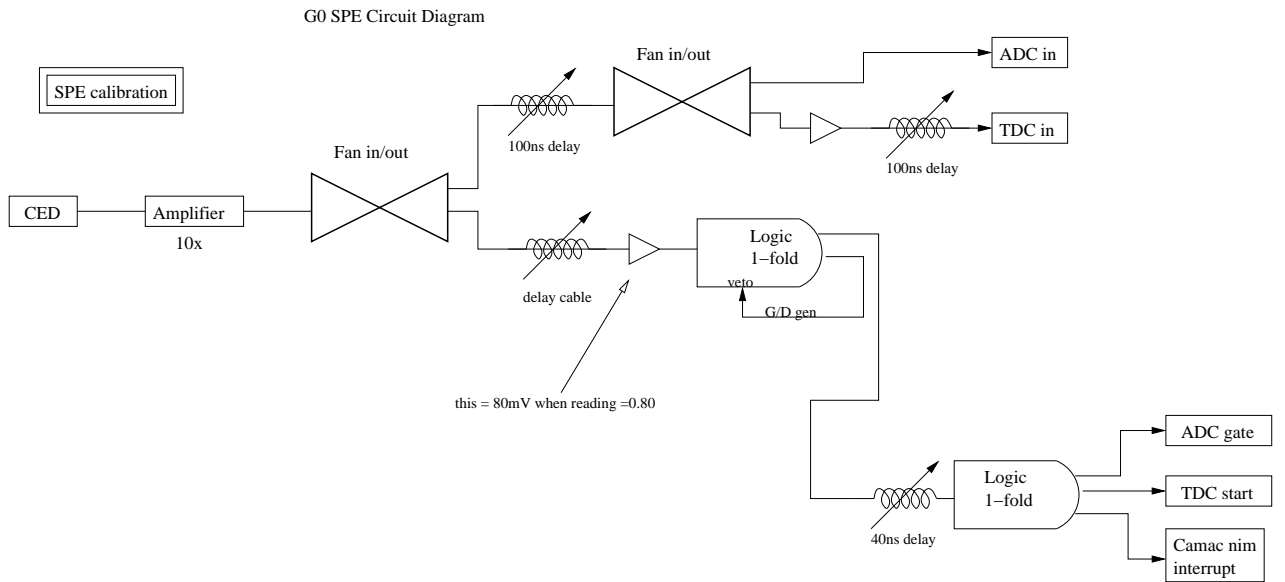
G0 SPE Circuit Diagram

Figure 4.2: Electronic diagram for Single Photoelectron data-taking.

1-fold logic gate is to prevent a second signal from the PMT generating a second event that would confuse the electronics and distort the data. After the ADC, TDC are read and cleared, and the veto can end.

Chapter 5

Data Type and Analysis of Octant 7 CEDs $8 \rightarrow 5$

5.1   Cosmic Rays

In the G^0 backward angle experiment, so far, we have used cosmic rays to test the performance of the CED scintillators. Cosmic rays are high-energy charged particles that travel at nearly the speed of light and strike the Earth from all different directions. They include pions (which quickly decay to produce muons, neutrinos and gamma rays), as well as high-energy electrons and positrons produced by muon decay and gamma ray interactions with atmospheric atoms. Since cosmic rays at ground level are mainly high-energy muons, which are minimum ionizing particles, they are used as the useful test particles. The energy loss for a minimum ionizing particle per unit path length is small, typically a few MeV per unit cm material. Detected scattered electrons in the G^0 will also be minimum-ionizing.

5.2   PMT calibration

The purpose of cosmic ray data is to study the behavior and performance of the detectors and photomultiplier tubes. In order to get a similar response from each octant, we had to assure that each of the PMTs have similar gain. We accomplished

this by adjusting the high voltage settings of each PMT. The high voltage was adjusted using the signal of the single photoelectron and cosmic signal seen on an oscilloscope.

5.3   Single Photoelectron Data

The Single PhotoElectron (SPE) run was conducted after the adjustment of the high voltages of the PMT tubes, and due to the electronics setup, it had to be performed one PMT tube at a time. With a SPE run we are able to find the SPE pulse hight for each PMT tube. For us the most important data from a SPE run are the pedestal and the SPE peak. We used a Gaussian fit for SPE and the pedestal peaks for each PMT. The difference between the SPE peak and pedestal peak locations were used to determine the number of photoelectrons, produced by minimum-ionizing particles, as discussed below.

5.4   Cosmic Ray Data

As light propagates through the scintillator it experiences light attenuation. Light attenuation determines how fast the light intensity decreases with distance from one end of the scintillator. As mentioned, the main purpose of the scintillator is to detect minimum-ionizing radiation. Cosmic rays are minimum-ionizing particles with very small energy loss per unit pathlength. In the G^0 cosmic runs the time of ionizing radiation detected by CEDs is recorded by TDCs. The cosmic ray data is conducted with up to four CEDs or eight PMTs at the time, because of the limited size of the trigger paddles, which could not cover all eight CEDs at once. We usually divided the octants and tested separately the top half and the bottom half of the CEDs in octant. In the Fig. 5.1 we plotted TDC0[0] and TDC0[1] of the CED5. In theory this difference should be a peak centered in zero, because of geometry of the scintillator itself, however, due to cable delays the difference of TDC's is not zero.

TDC0[0] is the time it takes a particle to reach the left side (or the right) of the scintillator. Similarly TDC0[1] will be the time it takes an other particle created or fired at the same time and the same place as the first one to reach the other end of the scintillator. If a particle comes from the center of the scintillator the TDC difference should be close to zero. If it comes from the left side, this means that TDC0[0] is shorter than TDC0[1], because it takes less time for the particle to go to the left than to the right, and vice versa. Therefore, we divided our domain into four regions to see if we do have the symmetry required for our detection. If the scintillating material is homogeneous it should take the same time for two particles in a symmetrical sides to arrive to symmetrical end, and the number of created photo-electrons from two symmetrical places should be close.

In order to achieve the symmetry about zero we had to introduce the constant Δt that would shift our histogram horizontally. When the mean value of the graph was approximately close to 0, we could divide histogram domain into four regions.
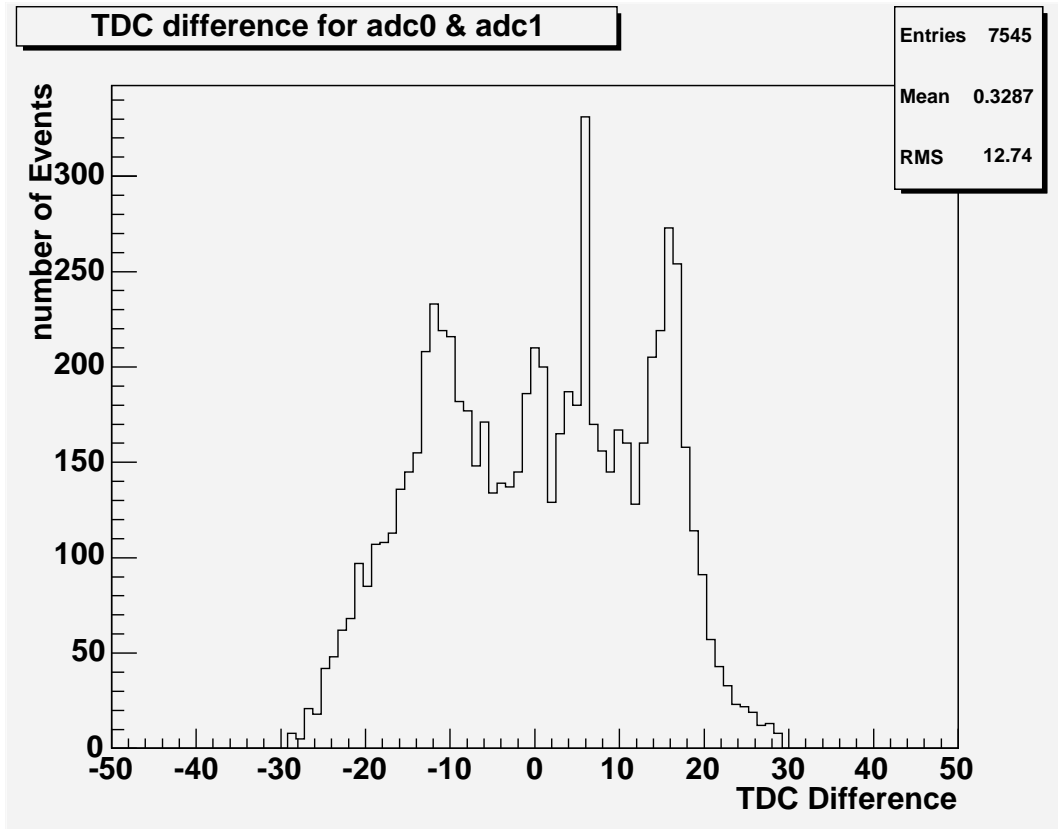
Figure 5.1: Octant 7 CED5. The difference of TDC0[0]-TDC0[1] $+ \Delta$ x .

Based on the histogram in Figure 5.1 we defined four regions. According to the relative pulse hight in each region we were able to find the dynamic range. The dynamic range is the ratio between the largest and the smallest values of the cosmic peaks in each region. Hence, the value of the dynamic range for CED5R and CED5L is the same.

From the Table 5.1 we can note that in most cases the number of Photoelectrons is $\sim$ 100. This is very good, because the minimum acceptable number of photoelectrons is $\approx$ 25-30. The Figures 5.2 and 5.3 are histograms with the relative pulse heights for different regions.

Range	CED5R pulse height	Pulse height PE	CED5L pulse height	Pulse height PE
13.5- 27	126.6	98	186.5	288
0-13.5	166.5	156	172.3	260
-13.5-0	225.5	238	125.7	168
-27—-13.5	270.5	301	89.35	96

Table 5.1: Octant7 CED5R and CED5L. Four regions and their relative pulse heights (channels).
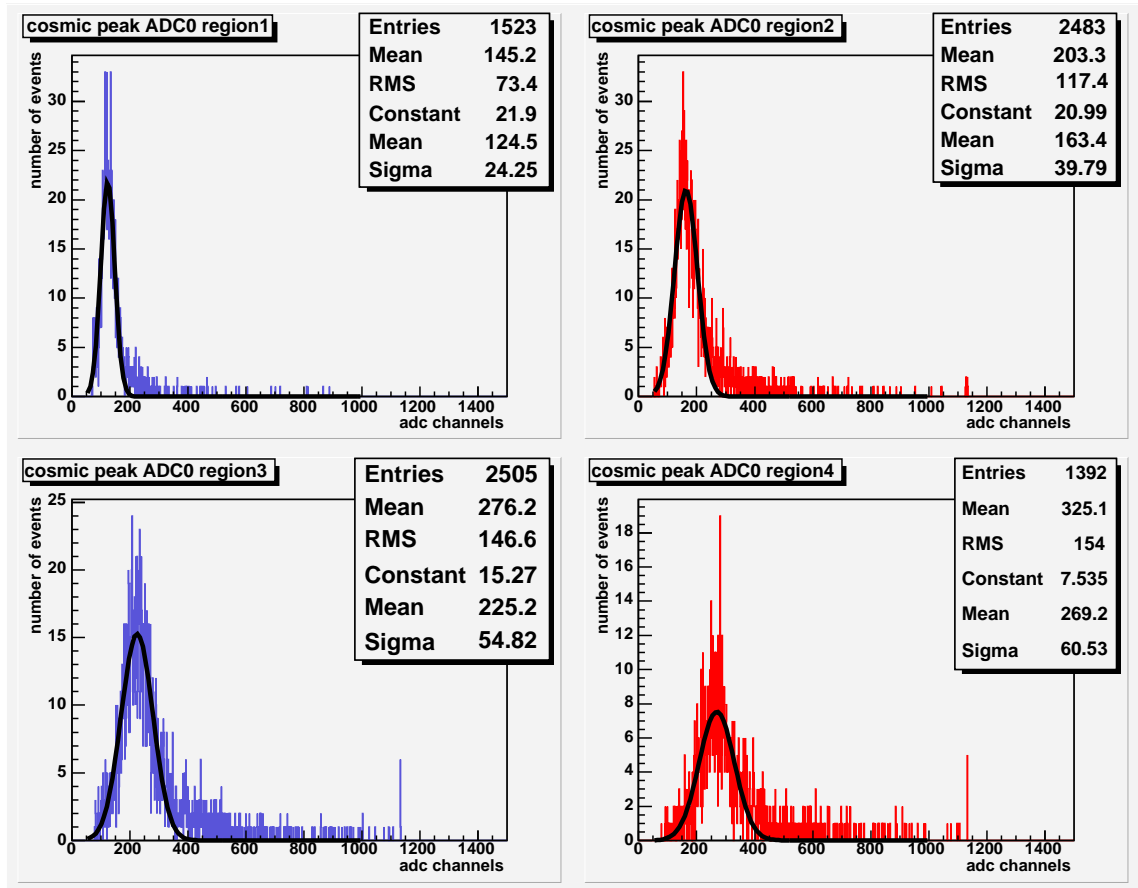

Figure 5.2: CED5R ADC0 cosmic peaks in four regions. The cosmic peak is increasing as the region number increases. Thus, the highest peak for ADC0 is in the region four, which means that the light intensity is the greatest in that region, and the region is on the right side of detector 5.
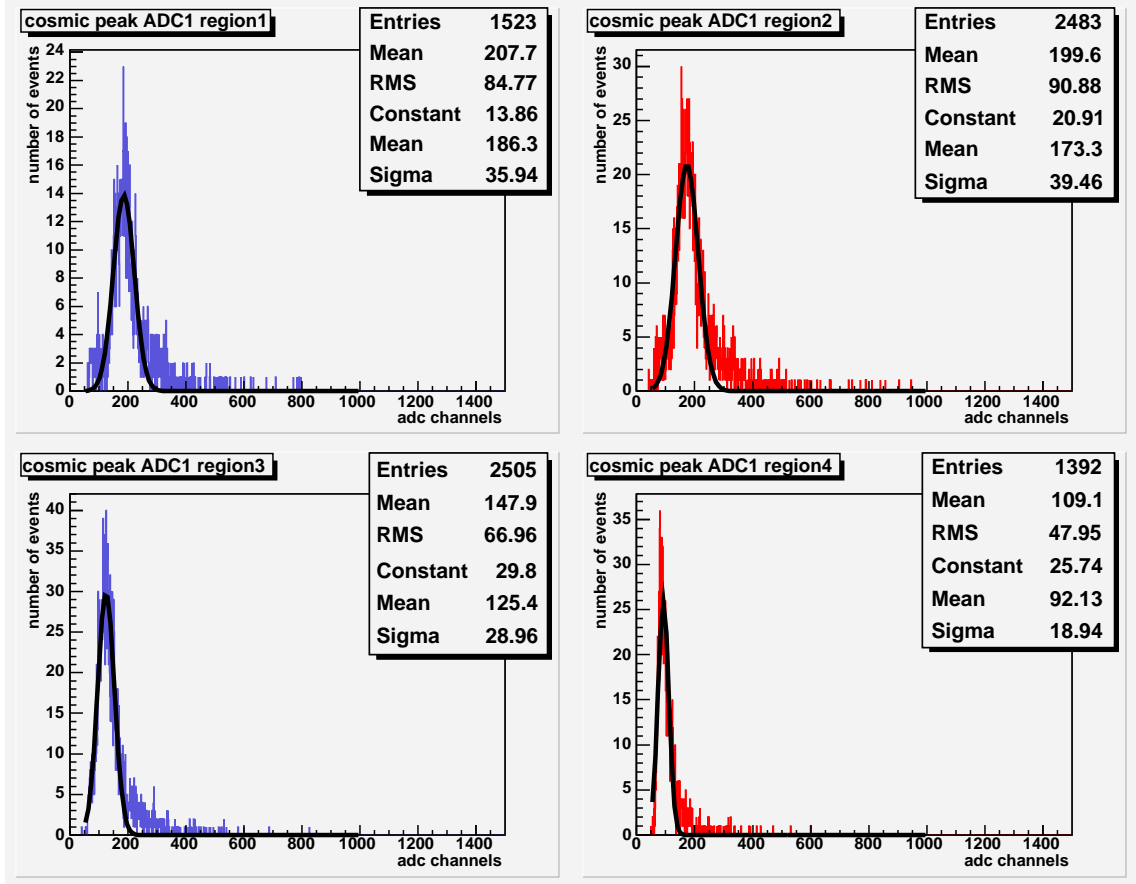
Figure 5.3: CED5L ADC1 cosmic peaks in four regions. The cosmic peak is decreasing as the region number increases. Thus, the highest peak for ADC1 is in the region one, which means that the light intensity is the greatest in that region, and the region is on the left side of detector 5.

The second technique that we used to study the behavior of scintillating detectors was based on the fact that light attenuation should obey the exponential law

$$N = N_0 e^{-mx},$$

where m is a linear attenuation coefficient and N_0 is a constant.

In Fig. 5.4 for Octant5, the light attenuation appears to roughly obey the exponential law, however, due to the crazing of scintillators and huge light leak of the first four detectors the attenuation coefficients m were very large. The slope of each

histogram should be as small as possible if the scintillator was in the good shape. The possibility for the bad condition of Octant5 is that it was the first octant assembled. The scintillators for Octant5 had to be replaced and the data had to be repeated.
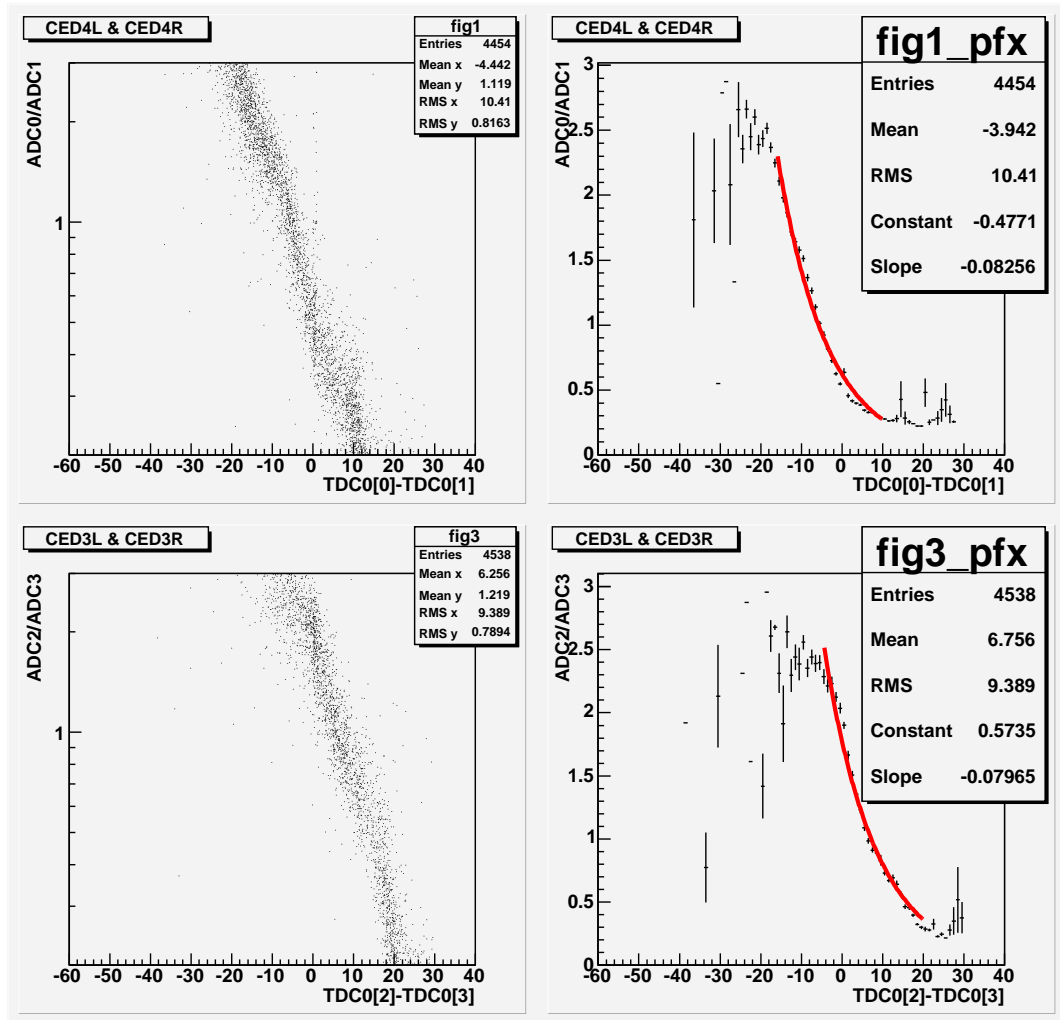

Figure 5.4: Octant5 CED4 and CED3 light attenuation. The first and the third histograms are 2D histogram for CED4 and CED3 and the second and the fourth are the projections of 2D histograms.

Figure 5.5 shows the new data for Octant5 after replacing the first four detectors.

As we can see that the slope is smaller by a factor of 2 after we replaced scintillating detectors and there is consistency between the slope for both detectors. In the
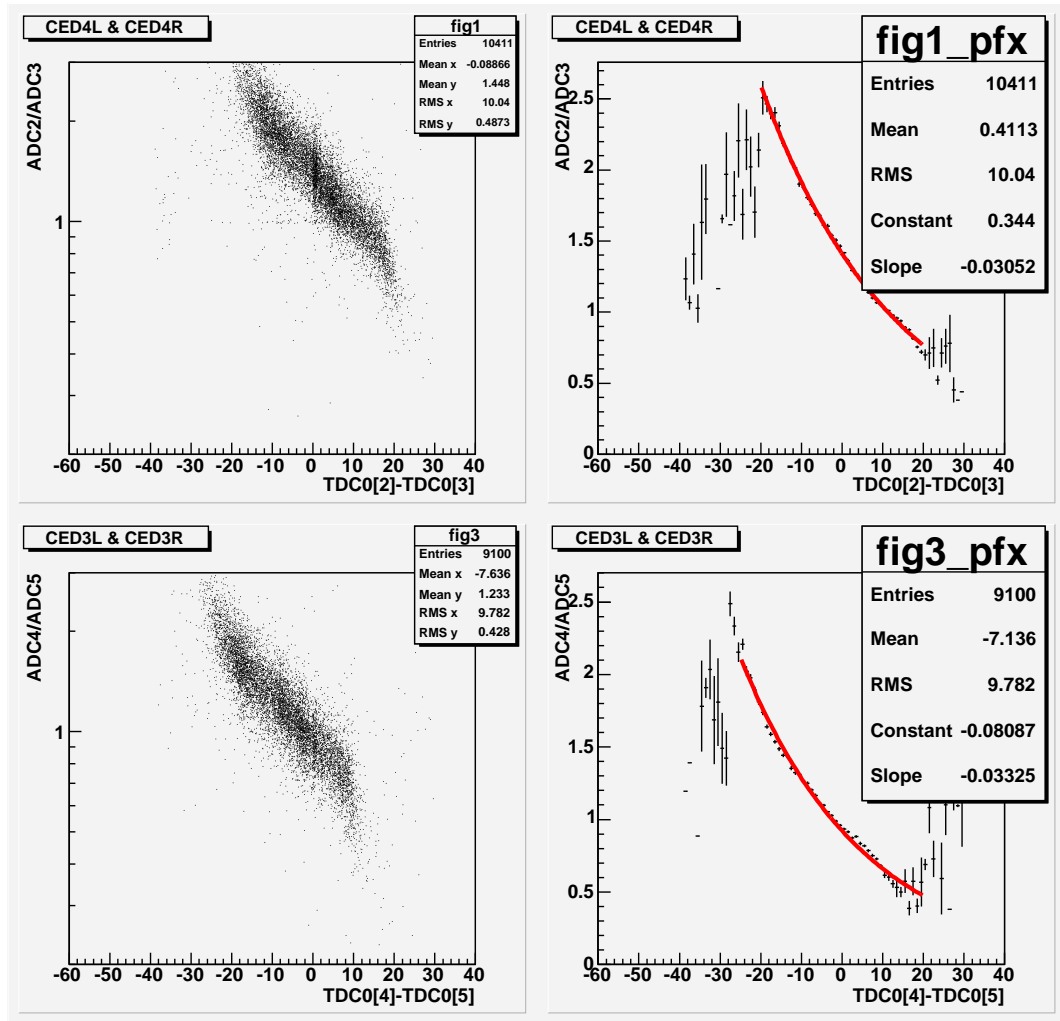
Figure 5.5: Octant5 CED4 and CED3 light attenuation. The first and the third histograms are 2D histogram for CED4 and CED3 and the second and the fourth are the projections of 2D histograms.

histogram attenuation slope is represented in number per channels what can be represented in meters. Hence, the attenuation length in the Figure 5.1 would be about 0.63 meters or 63cm.

Chapter 6

Conclusion

We completed all construction of CED, light guide, PMT assembly. We are still testing CEDs and all 8 octants for: light output, variation of light output along length of CED, and time resolution. In addition, from the Table in appendix we can see that the light attenuation slopes not different one from another. The range of attenuation slopes is from -0.01 to -0.090, which is approximately equal to range from 190cm to 21cm in attenuation length. The slopes are consistent with exponential dependence and they seem to be reasonable. In addition, we can see from the example for the Octant5 how important surface quality (crazing) is for the performance of the detectors.

Appendix A

Attenuation slopes table for eight Octants

The following is the Table of attenuation slopes m for different Octants

Table A.1: Attenuation Slopes for all eight Octants.

	CED1	CED2	CED3	CED4	CED5	CED6	CED7	CED8
Octant1	-0.048	-0.061	-0.038	-0.038	-0.057	-0.046	-0.074	-0.041
Octant2	-0.038	-0.046	-0.056	-0.038	-0.039	-0.042	-0.040	-0.040
Octant3	-0.045	-0.041	-0.039	-0.043	-0.045	-0.044	-0.050	-0.044
Octant4	-0.090	-0.045	-0.038	-0.071	-0.038	-0.039	-0.034	-0.083
Octant5	-0.073	-0.078	-0.079	-0.083	-0.075	-0.056	-0.046	-0.082
Octant5 after	-0.033	-0.034	-0.033	-0.031	-0.075	-0.056	-0.046	-0.082
Octant6	-0.039	-0.044	-0.038	-0.044	-0.042	-0.045	-0.033	-0.038
Octant7	-0.079	-0.073	-0.566	-0.067	-0.042	-0.010	-0.069	-0.054
Octant8	-0.091	-0.065	-0.054	-0.026	-0.065	-0.045	-0.042	-0.038
Avg. slopes	-0.069	-0.062	-0.054	-0.054	-0.051	-0.051	-0.049	-0.055

Bibliography

[1] Perkins, Donald H. Introduction to High Energy Physics. 3rd ed. Menlo Park: Addison-Wesley, 1987.

[2] I.S.Hughes., Elementary Particles, Cambridge University Press. Cambridge. (1991).

[3] Jefferson Lab PAC Jeopardy Proposal G^0 Experiment (E91-017), 1998. D.Beck et al. (unpublished).

[4] Knoll, Glen F., Radiation Detection and Measurement, (John Wiley & Sons, Inc.,New Jersey, 1990).